Geometric bed roughness and the bed state storm cycle

Alex E. Hay[1]

Received 5 October 2010; revised 21 December 2010; accepted 19 January 2011; published 16 April 2011.

[1] Temporal variation in the geometric roughness of the mobile sandy seabed during wave forcing events is investigated as a function of bed state. The bed states include irregular ripples, cross ripples, linear transition ripples, and flat bed, each appearing repeatedly within a different range of wave energies, as part of the bed state storm cycle. Ripple wavelengths determined from ensemble-averaged roughness spectra indicate that irregular and cross ripples are suborbital, whereas linear transition ripples are anorbital. The observed ripple steepnesses indicate that irregular and linear transition ripples fall slightly below Nielsen's (1981) field data relation, whereas cross ripple steepnesses are anomalously low in comparison. Time series of geometric roughness are coherent across spatial frequency. Abrupt changes in geometric roughness occurred on timescales of ~3 h on average during both the onset and the waning stages of storm events: i.e., for both decreasing and increasing roughness, respectively. Predicted response times, based on ripple volume and bed load transport rate, are in agreement with the observations when the best fit form of the Meyer-Peter and Müller (1948)-type bed load relation obtained by Ribberink (1998) is used. In contrast, the more standard form of this relation and the associated parameters yield predicted response times much shorter than those observed.

Citation: Hay, A. E. (2011), Geometric bed roughness and the bed state storm cycle, *J. Geophys. Res.*, *116*, C04017, doi:10.1029/2010JC006687.

1. Introduction

[2] The purpose of the present paper is to investigate the covariation of geometric bed roughness and bed state in the nearshore zone during wave forcing events. In keeping with the discussion by *Schlichting* [1979, pp. 615–625], the term "geometric roughness" is used to distinguish the physical dimensions and spacing of bed roughness elements from the hydraulic roughness. Thus, for a rippled seafloor, measures of both ripple height and wavelength are required to characterize the geometric roughness. In the remainder of the paper, unless otherwise indicated, the term "roughness" refers to "geometric roughness."

[3] Different characteristic ripple types, defined in part by their geometric pattern in plan view, are observed in nearshore sands [e.g., *Clifton*, 1976]. Each ripple type, and flat bed, represents a different "bed state". The bed state storm cycle is the temporal analog of *Clifton*'s [1976] spatial progression of bed states across the shoreface, which he based on diver observations of ripple types during nonstorm conditions. The existence of a temporal cycle during wave forcing events at fixed positions on the shoreface was first indicated in acoustic seabed imagery for single storm events from beaches in Lake Huron [*Hay and Wilson*, 1994] and Nova Scotia [*Smyth et al.*, 2002] and was demonstrated conclusively by *Hay and Mudge* [2005] using 2.5 months of nearly continuous sonar imagery from the beach at Duck, North Carolina. The essential nature of the cycle involves a temporal progression through a sequence of canonical ripple types as wave energy increases during the early stages of a storm event, culminating in flat bed at high wave energy, which is then followed by the reverse sequence as wave energy decreases during the waning phase of the event. In his conceptual model of the spatial progression, *Clifton* [1976] ascribed an important role to wave nonlinearity. The data on wave statistics available to *Clifton* [1976] were rather limited, however, and in contrast the more comprehensive data on the temporal progression indicate that bed state occurrence depends primarily on wave energy, and that wave nonlinearity is relatively unimportant [*Hay and Mudge*, 2005].

[4] The repeatability of the cycle among storms, together with its occurrence at different nearshore locations, indicate that predicting bed state from first principles may eventually be possible, and certainly this repeatability represents a benchmark against which such predictive models might be tested. The primary dependence on wave energy (for a given grain size) is a useful simplification and, since wave energy and bed shear stress are closely related, this dependence highlights bed shear stress as an essential component of the physics of the process. The dependence of bed state on bed shear stress, however, also underscores the fact that ripple pattern, by itself, is insufficient. Quantitative measures of the geometric roughness of the bed are needed to validate models of bed evolution during storms.

[1]Department of Oceanography, Dalhousie University, Halifax, Nova Scotia, Canada.

0148-0227/11/2010JC006687

[5] The bed states considered here are, in order of increasing wave energy associated with their occurrence [*Hay and Mudge*, 2005]: irregular ripples, cross ripples, linear transition ripples, and flat bed. Note that lunate megaripples are not considered, for reasons discussed later. In addition to quantifying the roughness scales characteristic of these different states, roughness time series are used to determine the timescales of mobile bed adjustment, which are then compared to values predicted using a stress-based transport model. Also, as the roughness estimates are based on bed profiles determined using rotary sonars, the paper addresses issues concerning the shape of the bed elevation spectrum determined with these devices.

[6] The order of presentation is as follows. The relevant aspects of the SandyDuck97 field experiment and data are briefly summarized in section 2. The roughness results are presented in section 3. In section 3.1, time series of bed elevation variance in low-, middle, and high-(spatial) frequency bands are presented relative to the time series of wave forcing and bed state. Bed elevation spectra for the different bed states are presented in section 3.2, and ripple wavelengths, heights, and steepnesses in section 3.3, thereby identifying the different rippled bed states as orbital, suborbital, or anorbital ripple types. Ripple steepnesses are compared to the values expected on the basis of *Nielsen*'s [1981] empirical relations. In section 3.4, observed bed roughness adjustment times are compared to predicted adjustment times based on bed load transport rates computed using the *Meyer-Peter and Müller* [1948] relation in both the standard and *Ribberink*'s [1998] best fit forms. Section 4 is the discussion and includes comparisons to previous work. In particular, the discussion resolves an apparent contradiction between (1) the above mentioned repeatability of the bed state storm cycle as a function of wave energy and the associated repeatable variations in geometric roughness (presented here) and (2) the *Gallagher et al.* [2003] finding that the mobility parameter was a poor predictor of RMS roughness in their data. A model for elevation profile measurement in sandy sediments using MHz frequency rotary sonars is presented in Appendix A and is used to provide a semiquantitative explanation for effect of such measurements on the shape of the bed elevation spectrum at high spatial frequencies. The conclusions are presented in section 5.

2. Field Site and Data

[7] SandyDuck97 took place from August to November 1997 at the U.S. Army Corps of Engineers Field Research Facility (FRF) in Duck, North Carolina (see *Birkemeier et al.* [1985] for a detailed description of the FRF site). The results presented here are from instrument frames C and D located 160 and 200 m seaward of the mean shoreline (i.e., 270 and 310 m in the FRF coordinate system). The depths (relative to NGVD) at these two locations remained approximately constant: 3.36 ± 0.05 m and 3.29 ± 0.05 m at C and D, respectively. The median grain size of the bottom sediments was close to 150 μm at both locations. Images of the seabed and cross-shore bed elevation profiles were acquired with 2.25 MHz rotary fan beam and pencil beam sonars (transducers ~0.75 m above the bed) at 30 min intervals between storm events and 10 min intervals during storms. The fan beam sonar transducer rotated about a vertical axis, providing a 360° side scan image of the seafloor extending out to 5 m range: these images were used for bed state characterization, as discussed by *Hay and Mudge* [2005]. In contrast, the pencil beam sonar transducer rotated about a horizontal axis, so that the axially symmetric acoustic beam (which is conical in the far field) swept through a vertical plane in the cross-shore direction. These resulting profiles of backscatter amplitude versus range and beam training angle provide the cross-shore profiles of bed elevation which are the basis of the results discussed here. Water velocities were measured using Marsh-McBirney EM flowmeters located ~0.35 m above the bed. The flowmeters were sampled at a rate of 2 Hz in half hour intervals continuously. Further details are given by *Henderson and Bowen* [2002] and *Hay and Mudge* [2005].

[8] The focus of this paper is on the bed profiles obtained with the pencil beam sonars. The range to the seabed, r_b, was defined to be the amplitude-weighted average range within the range interval containing the bottom echo, i.e.,

$$r_b = \frac{\sum_j r_j B_j}{\sum_j B_j}, \tag{1}$$

where B_j represents the backscatter amplitude in the jth range bin. From the training angle $\phi_\circ$ of the sonar beam relative to the vertical, bed elevation profiles, $\eta(x)$, were determined from $r_b(\phi_\circ)$, i.e., $\eta(x) = r_b(0) - r_b(\phi_\circ)\cos\phi_\circ$; $x = r_b(\phi_\circ)\sin\phi_\circ$, where x is the local, positive shoreward, cross-shore coordinate (see Appendix A for a sketch of the geometry). Bed elevation spectra, $S_{\eta\eta}$, were computed from the elevation profiles for different x intervals, after interpolating to a uniform sampling interval, δx. Because the transducer rotates through a fixed angular step, $\Delta\phi_\circ$, the actual sample interval, Δx, increases with $|x|$ and thus the effective Nyquist frequency decreases as the maximum value of $|x|$ included in the profile increases. Since the sonar height was typically 0.75 m, and $\Delta\phi_\circ$ was 0.45° for this experiment, the maximum possible resolution in x would be about 0.6 cm. However, the finite width of the sonar beam effectively acts as a low-pass filter, and the maximum resolvable spatial frequency is less than 30 cycles per meter (cpm), as is shown later.

[9] Spectra were computed for the three x intervals listed in Table 1. To avoid possible contamination of the bed profiles by frame-induced disturbances, the x intervals extend no farther shoreward than x = 0.5 m. Given the above discussion, the spectra for the shortest interval yield the best estimates at the highest spatial frequencies, but do not resolve the lower frequencies. The spectra were computed for each interval using Hanning-windowed and linearly detrended data segments, each segment length equal to 1/3 the length of the corresponding x interval, with 70% overlap. Thus, the number of degrees of freedom for the individual spectra in each of the three x intervals is the same, and equal to 10 [*Nuttall*, 1971]. Consequently the 95% confidence intervals for a single spectrum span $0.47S_{\eta\eta}(f)$ to $2.92\ S_{\eta\eta}(f)$ [*Jenkins and Watts*, 1968]. In order to obtain narrower confidence

Table 1. Spatial Frequency Bands and x Intervals for the RMS Roughness Estimates

Band	f_c (cpm)	f Range (cpm)	x Range (m)
Low	2.5	$1 \leq f \leq 4$	$-3.5 \leq x \leq 0.5$
Middle	7	$4 \leq f \leq 10$	$-2.2 \leq x \leq 0.5$
High	15	$10 \leq f \leq 20$	$-0.5 \leq x \leq 0.5$

intervals, the spectra were ensemble averaged over multiple occurrences for each bed state (see section 3.2).

3. Results

3.1. Forcing Conditions, Bed State, and Band-Passed Bed Roughness

[10] Time series of RMS wave orbital velocity, the band-passed roughness variances, and all five principal bed states identified by *Hay and Mudge* [2005], including lunate megaripples, are shown in Figure 1 for instrument frame C. The results for frame D are similar, and are not shown. These data illustrate that (1) the σ_η^2 time series are coherent across the 3 frequency bands; (2) σ_η^2 was low during flat bed and linear transition ripple (LTR) occurrences; (3) roughness variance was high for irregular ripple and cross-ripple bed states; and (4) roughness variance decreased with increasing spatial frequency. Quantifying the first point, the interband correlation coefficient, R, ranged from 0.46 to 0.65 at frame C. The σ_η^2 time series for a given band were also coherent between the two frame locations, with R ranging from 0.44 to 0.79 across the three bands. The average values of σ_η in each band are listed in Table 2, illustrating the decrease in RMS bed roughness with increasing spatial frequency for all four bed states.

[11] The evolution of bed roughness through a sequence of 4 storm events is illustrated in Figure 2. Note the characteristic bed state storm cycle in Figure 2a: irregular ripples at low wave energies, then cross ripples as the wave energy increases (provided the increase was not too rapid for the bed to respond), then LTRs, and then flat bed at the highest wave energies, followed by the reverse sequence as the waves decay. The bed roughness time series in Figures 2b–2d indicate a general tendency for σ_η^2 to be high in all 3 bands when irregular ripples or cross ripples were present. There are four exceptions. The first is the spike in roughness in the

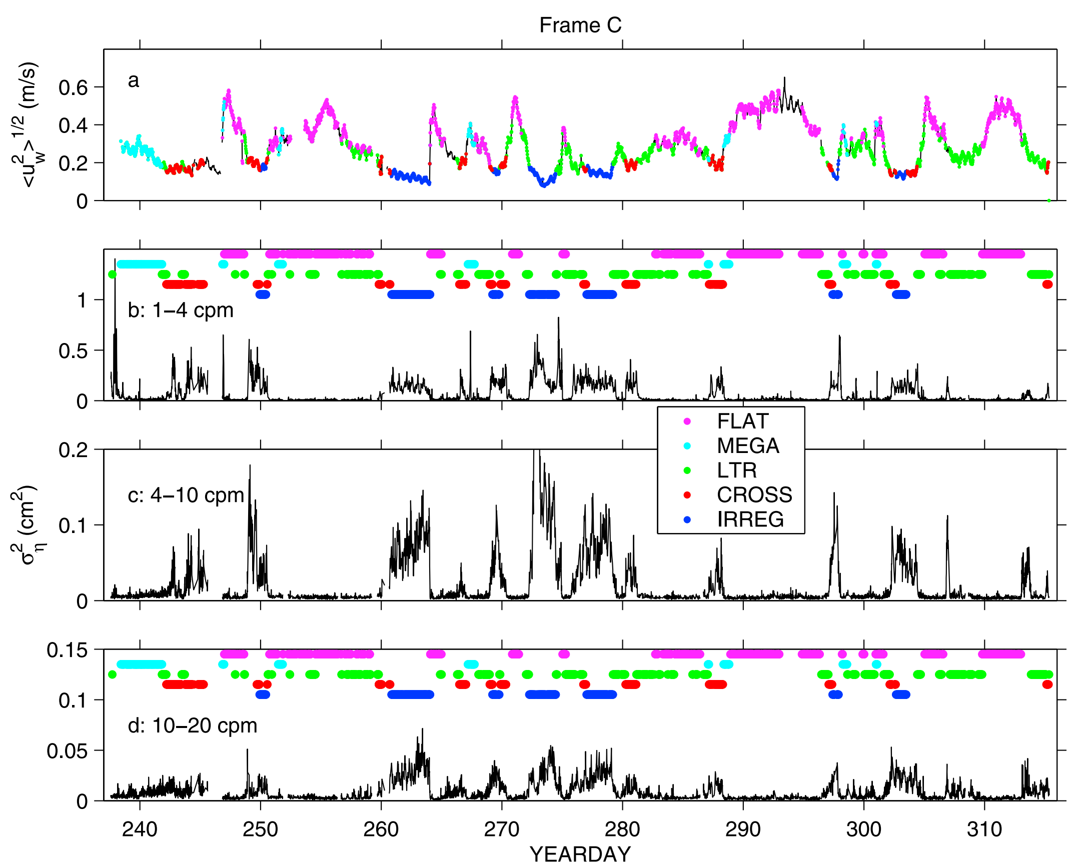

Figure 1. Time series of wave forcing, bed state, and bed roughness, the latter partitioned into three spatial frequency bands, during the 75+ day course of the experiment. (a) Root-mean-square (RMS) wave orbital velocity; (b, c, and d) roughness variance, σ_η^2, in the three spatial frequency bands indicated (see also Table 1). As per the legend, colored dots indicate different bed states: irregular ripples (dark blue); cross ripples (red); linear transition ripples (green); lunate megaripples (light blue); and flat bed (magenta). To help guide the eye, the bed state occurrences are repeated in Figures 1b and 1d. Data are from frame C.

Table 2. RMS Band-Passed Roughness, σ_η, in the Three Spatial Frequency Bands Versus Bed State[a]

	Irregular	Cross	LTR	Flat
		Frame C		
N	490	647	1137	2184
σ_{Lo}, cm	0.41 ± 0.087	0.40 ± 0.13	0.15 ± 0.074	0.096 ± 0.029
σ_{Mid}, cm	0.29 ± 0.077	0.16 ± 0.054	0.084 ± 0.027	0.064 ± 0.012
σ_{Hi}, cm	0.16 ± 0.033	0.11 ± 0.028	0.085 ± 0.025	0.050 ± 0.010
		Frame D		
N	449	671	1639	2162
σ_{Lo}, cm	0.38 ± 0.066	0.36 ± 0.13	0.13 ± 0.074	0.086 ± 0.031
σ_{Mid}, cm	0.25 ± 0.046	0.14 ± 0.046	0.066 ± 0.021	0.059 ± 0.015
σ_{Hi}, cm	0.15 ± 0.027	0.10 ± 0.025	0.070 ± 0.021	0.053 ± 0.015

[a] N is the number of elevation profiles, for each bed state and each instrument frame, upon which the values of σ_η are based.

low-frequency band in Figure 2b on year day (YD) 267. This spike is due to a lunate megaripple, which was observed for a much longer period of time in the fan beam imagery (as indicated by the light blue dots), but which migrated comparatively quickly out of the cross-shore line swept by the pencil beam. The other three exceptions are indicated by the arrows. That in Figure 2c on YD273 is associated with the deposition of a 10 cm thick layer of mud which was later swept away. The other two exceptions involve increases in roughness in the low-frequency band (Figure 2b). Usually, an increase in the low-band variance coincided with the appearance of irregular or cross ripples. This was the case for the second of the two indicated time periods: on reviewing the imagery, cross ripples were present at this time (the bed state database has been corrected since). The first arrow, however, corresponds to the occurrence of oblique long-wavelength ripples (oLWRs) which appear to be related to cross ripples [*Alcinov*, 2009].

[12] The σ_η^2 time series in Figures 1 and 2 exhibit abrupt changes in roughness, many of which are simultaneous across the three frequency bands. *Abrupt decreases* in roughness are not unexpected in this data set, as wave energy typically increased rapidly at the onset of storms, as on YD262 for example. During the waning stages of forcing events, however, wave energy decay was often rather slower. Nonetheless, *abrupt increases* in σ_η^2 occurred during storm decay. These increases are particularly evident in the

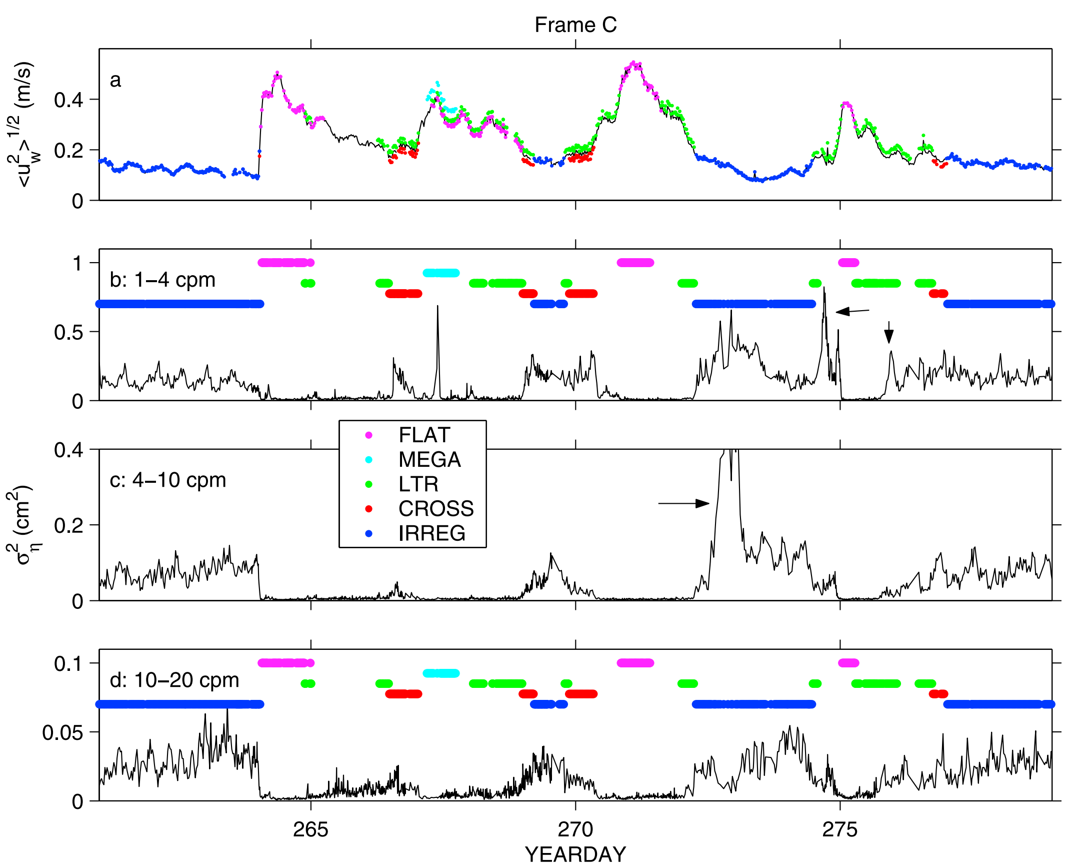

Figure 2. Expanded view of Figure 1, illustrating the evolution of roughness and bed state during the succession of four storm events from YD261 to YD279. Unlike Figure 1, the colored dots indicating lunate megaripples, linear transition ripples, and cross ripples have been offset in the vertical to make evident when these bed states co-occurred. Such co-occurrences were excluded from the analyses, as indicated by the colored dots in Figures 2b and 2d except in the case of cross ripples, for which co-occurrences with LTRs were allowed. Note the tendency for the roughness in all three bands to be high, and at about the same value, when irregular ripples or cross ripples were present. The arrows indicate three exceptions: these are discussed in the text.

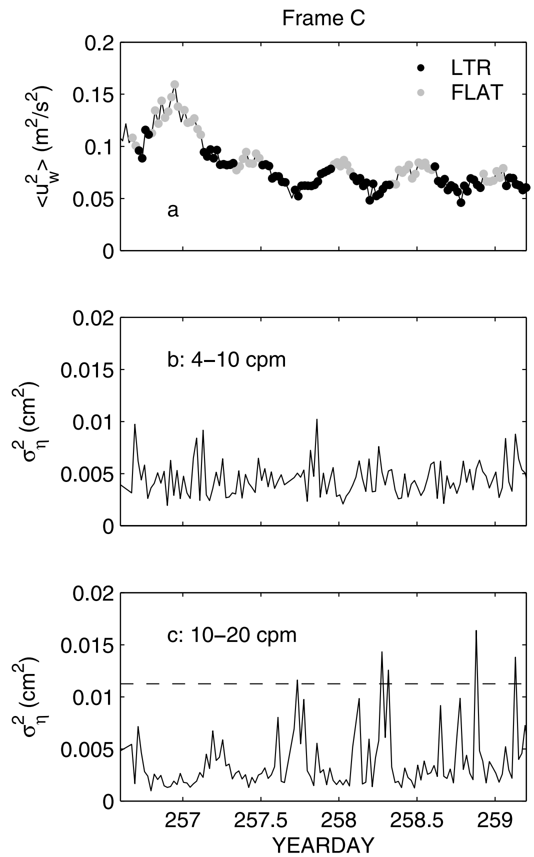

Figure 3. Tidally modulated high wave energy bed states and the corresponding roughness variances in the midfrequency and high-frequency bands. (a) RMS wave orbital velocity, overlaid by flat bed and linear transition ripple (LTR) occurrences; (b and c) roughness variance, σ_η^2, in the frequency bands indicated. Dashed line in Figure 3c is the variance corresponding to 3 mm high sinusoidal ripples. Data are from frame C.

low-band data (Figure 2b) and were associated with the appearance of either irregular or cross ripples.

[13] LTR wavelengths at frames C and D were ~7 to 8 cm [*Maier and Hay*, 2009], corresponding to spatial frequencies of 12 to 14 cpm, i.e., in the high-frequency band here. As Table 2 indicates, however, the values of σ_η for LTRs in this band are slightly above the flat bed values. The measurable difference between the LTR and flat bed states are also evident in the band-passed roughness time series, as Figure 3 demonstrates. Figure 3a shows the time series of wave orbital velocity (note the modulation at the period of the semidiurnal tide), with LTR and flat bed state occurrences (from the fan beam imagery) superimposed. Figures 3b and 3c show the roughness variance in the midfrequency and high-frequency bands: the latter exhibits clear tidal modulation, with lower variances associated with flat bed and higher variances associated with LTRs. *Crawford and Hay* [2001] obtained LTR heights of ~3 mm. As indicated by the dashed line in Figure 3c, many of the observed values of σ_η^2 during LTR occurrences fall below the equivalent variance for a 3 mm high sinusoid. Thus, while Figure 3 demonstrates that an LTR signal is registered in the rotary sonar bed profiles, it also indicates that this signal is likely somewhat attenuated.

[14] Band-pass-filtered bed profiles are presented in Figure 4 for the four bed states which are the focus of this paper: irregular ripples (Figure 4a); cross ripples (Figure 4b); linear transition ripples (Figure 4c); and flat bed (Figure 4d). The horizontal scales in Figures 4a–4d correspond to the range of x values over which σ_η^2 was computed in each band (see Table 1). The profiles in Figures 4a–4d are offset in the vertical by an amount proportional to the indicated time interval, Δt, between data runs. The irregular ripple and cross ripple profiles exhibit clear shoreward migration. In contrast, the LTRs could have been migrating either shoreward or seaward (view the plot at a low angle from the lower left and lower right corners) at a rate of approximately 1/2 wavelength in 10 min. The "flat" bed profiles indicate features with the same horizontal scale as LTRs, but with lower amplitudes. Some of these features are coherent between consecutive profiles, a fact indicating that in these cases the features are likely real. However, some of the features do not persist from one profile to the next, indicating that some of the variance in Figure 4d is almost certainly noise. (As one reviewer correctly pointed out, some of the transient features in Figure 4d might be associated with ripple features being created and then erased between runs, as has been reported for LTRs by *Dingler and Inman* [1977]. However, *Maier and Hay* [2009] searched the rotary fan beam imagery for unambiguous evidence of LTR formation and/or erasure on wave period timescales and were unable to find any. In contrast, the pencil beam data are affected by backscatter from high-concentration sediment plumes of sediment. These high-concentration plumes occur randomly in time relative to the sonar sweep cycle, and while their effects on the bed elevation profile are minimized by averaging over 5 consecutive sweeps before extracting the bed profile, they are a source of bed elevation noise.)

3.2. Observed Bed Elevation Spectra

[15] Bed elevation spectral densities, $S_{\eta\eta}$, were computed from the bed elevation profiles for the same ranges of x as the bandpass variances. The resulting spectra for frame C, averaged over all occurrences of each bed state, are presented in Figure 5. Also shown are the 95% confidence limits, based on the number N of realizations for each bed state (Table 2), and the previously mentioned 10 degrees of freedom per individual spectrum. These confidence intervals range from about ±4% to ±2% of $S_{\eta\eta}(f)$ for N between 450 and 2200. Features to note are (1) the red spectra (i.e., the spectral densities increase toward low frequencies) consistent with the bed roughness spectra from the nearshore zone reported by *Gallagher et al.* [2003]; (2) the higher spectral densities at midfrequencies (3 to 10 cpm) for irregular ripples compared to cross ripples; (3) $S_{\eta\eta}$ lowest for flat bed, at all frequencies below 15 to 20 cpm; (4) the peak in the LTR spectra at 14 cpm; and (5) the absence of any well-defined spectral peak for irregular and cross ripples. (The peak near zero frequency is an artifact associated with the choice of the segment lengths used to compute the spectra.) The absence of peaks in the irregular and cross ripple spectra is characteristic of the SandyDuck97 data: spectra averaged over 10 to 20 profiles (not shown) within a given occurrence event for these bed states are also relatively featureless. Note as

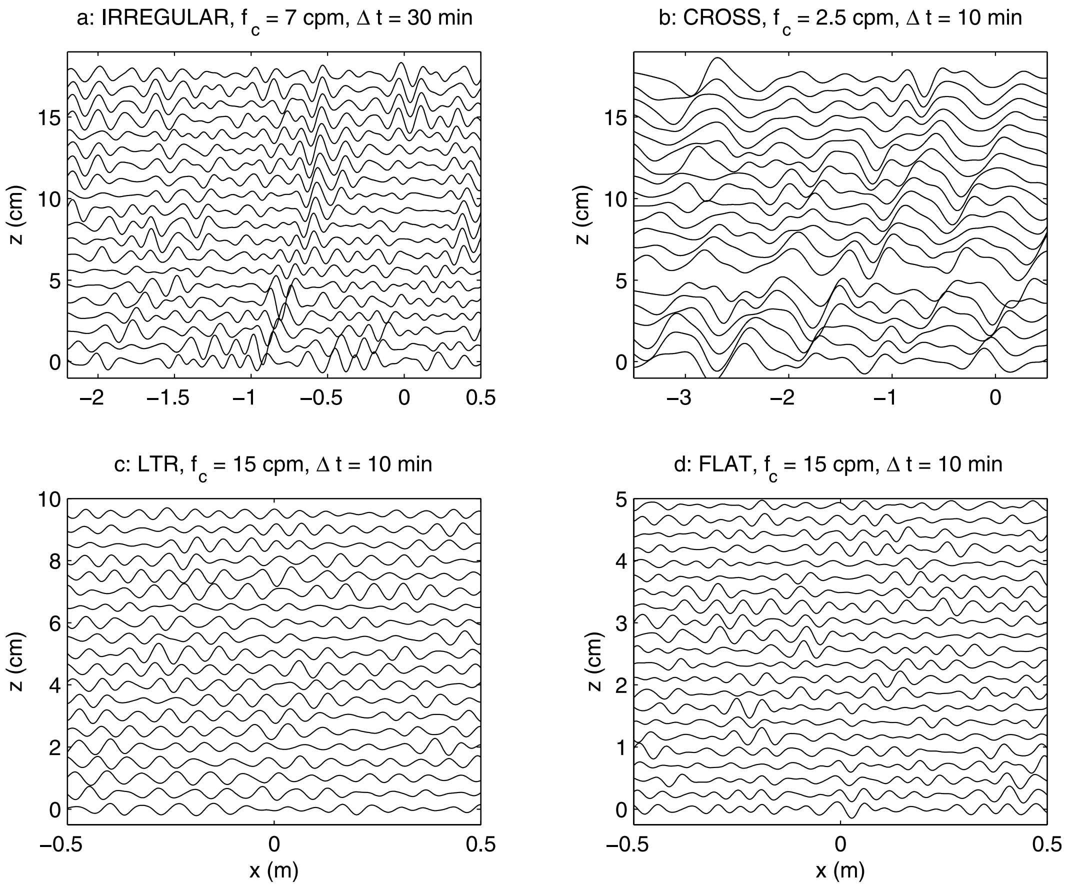

Figure 4. Time stacks of band-pass-filtered bed profiles versus bed state: (a) irregular ripples, YD262-263; (b) cross ripples, YD245-245.6; (c) linear transition ripples, YD307-308; and (d) flat bed, YD247-248. Note the differences in horizontal and vertical scales and the corresponding band-pass differences, indicated by the band center frequency, f_c. Note also that the time interval, Δt, between profiles was 30 min for the irregular ripples and 10 min for the other three bed states. Time increases from bottom to top; x is positive shoreward. Data are from frame C.

well the tendency at high frequencies for spectral densities to decrease as the length of the x intervals increases. This effect cannot be due simply to low-pass filtering associated with the finite beam width of the sonar, as the spectra for the different x intervals would then necessarily converge at high frequencies. The explanation involves a somewhat subtle interplay between the angle of incidence, the ripple profile, the transducer beam pattern, and the bottom detection algorithm (see Appendix A).

[16] In order to obtain spectra representative of the rippled bed states alone, the average flat bed spectrum was subtracted from the corresponding average spectrum for each rippled state. The resulting difference spectra are plotted in Figure 6 for both frames, and are comparable for the two locations. In order to reveal any power law dependence of $S_{\eta\eta}$ on f, these spectra are presented in variance-preserving log-log form. That is, letting σ_η^2 represent bed elevation variance, then $d\sigma_\eta^2(f) = S_{\eta\eta}(f)df$, and thus $fS_{\eta\eta}(f)d\ln f = d\sigma^2(f)$. Also shown in Figure 6 are solid lines representing an inverse-squared dependence of $S_{\eta\eta}$ on spatial frequency, corresponding to constant steepness ripples: that is, ripple height, $\eta_\circ$, proportional to $\lambda_\circ$ ($\lambda = 1/f$ being the ripple wavelength). While cross ripples tend to exhibit this behavior, irregular ripples do not (and LTRs, of course, are not expected to).

3.3. Ripple Height and Steepness

[17] Ripple heights were determined using

$$\eta_\circ = 2\sqrt{2}\sigma \tag{2}$$

where σ was obtained by integrating the spectra: i.e.,

$$\sigma^2 = \sum_j S_{\eta\eta}(f_j)\Delta f. \tag{3}$$

Ripple wavelength was determined from the energy-weighted average frequency,

$$f_\circ = \frac{\sum_j f_j S_{\eta\eta}(f_j)}{\sum_j S_{\eta\eta}(f_j)}, \tag{4}$$

yielding $\lambda_\circ = 1/f_\circ$.

[18] Note that equation (2) holds for sinusoidal ripples. As pointed out by a reviewer, the height would be 19% to 23% higher for sharp-crested ripples with triangular or parabolic shapes. However, because ripples under irregular waves

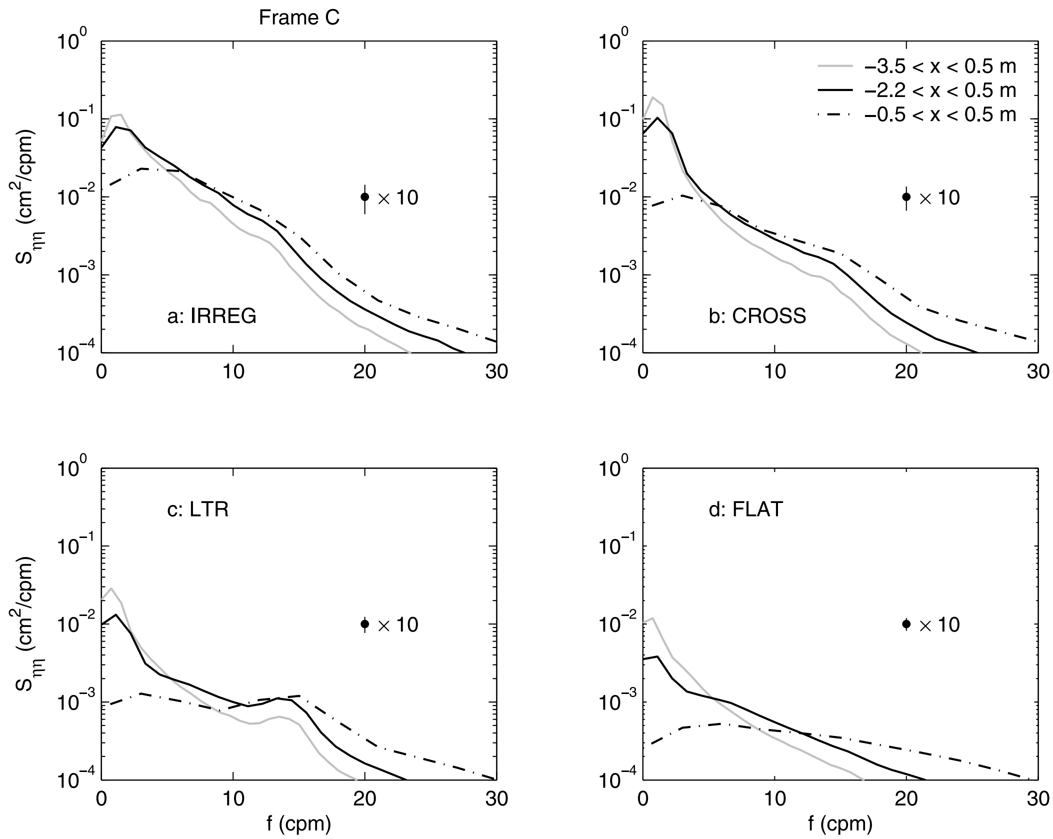

Figure 5. Average roughness spectra versus bed state: (a) irregular ripples; (b) cross ripples; (c) linear transition ripples; and (d) flat bed. Line types represent the x interval over which the spectra were computed, as indicated by the legend in Figure 5b. The error bars denote the 95% confidence intervals, magnified by a factor of 10. Data are from frame C.

tend to be round-crested [*Madsen et al.*, 1990], and because as shown later, the ripples in question here are suborbital and anorbital which tend to be rounder crested than orbital ripples, equation (2) is likely to be a reasonable approximation. Specifically, a round-crested but skewed ripple profile can be represented by

$$\eta(x) = \frac{\eta_0}{2}\sum_{j=1}^{5} \epsilon^{j-1}\cos jkx, \qquad (5)$$

where $k = 2\pi/\lambda$ and $\epsilon < 1$. Similarly, an asymmetric (i.e., sawtooth) profile is given by the same relation with cos replaced by sin. For ripple steepnesses $0.1 \leq \eta_\circ/\lambda \leq 0.2$, it is readily shown that $\eta_\circ/\sigma$ given by equation (2) underestimates the ripple height by less than 10% because the maximum slope along the profile is constrained to be less than the ~30° angle of repose.

[19] Equations (3) and (4) were evaluated using $S_{\eta\eta}$ from the low, middle and high x intervals in Table 1 for irregular ripples, cross ripples, and LTRs, respectively. Except for LTRs, the integration was over the entire spectrum. LTRs occupy a narrow range of wavelengths, as exhibited by the spectral peak at frequencies above 10 cpm in Figure 6, and as indicated by the rotary fan beam imagery from the same instrument frame locations [*Maier and Hay*, 2009]. Thus, the LTR estimates were obtained by restricting the range of integration to the region of the spectral peak, $10 < f < 20$ cpm.

[20] To investigate the variability of these estimates, the occurrences for each state were divided into subensembles of 10 occurrences each, with a maximum time between occurrences of 2h. The spectra for these subensembles were then averaged together. The number of subensembles satisfying these criteria is designated by N_E, and the resulting values (mean ± standard deviation) of wavelength, height and steepness are listed in Table 3. Consistent with the remark made earlier with respect to the spectra being similar for subsets of the data, the standard deviations are not very large, being typically less than ±20% for height and wavelength, and somewhat larger for steepness. For LTRs, rippled-minus-flat difference spectra were computed using the nearest average flat bed spectrum conditional upon the difference between the average times for the flat and LTR subensembles being less than 24 h. The corresponding values are listed as LTRb in Table 3. The flat bed spectrum subtraction was not done for the irregular ripple and cross ripple bed states because the low-frequency variations in the bed spectra, which dominate the variance for these bed states, are real (whereas the high frequencies are mainly noise).

[21] The wavelengths listed in Table 3 compare favorably to the values based on the rotary fan beam sonar data from

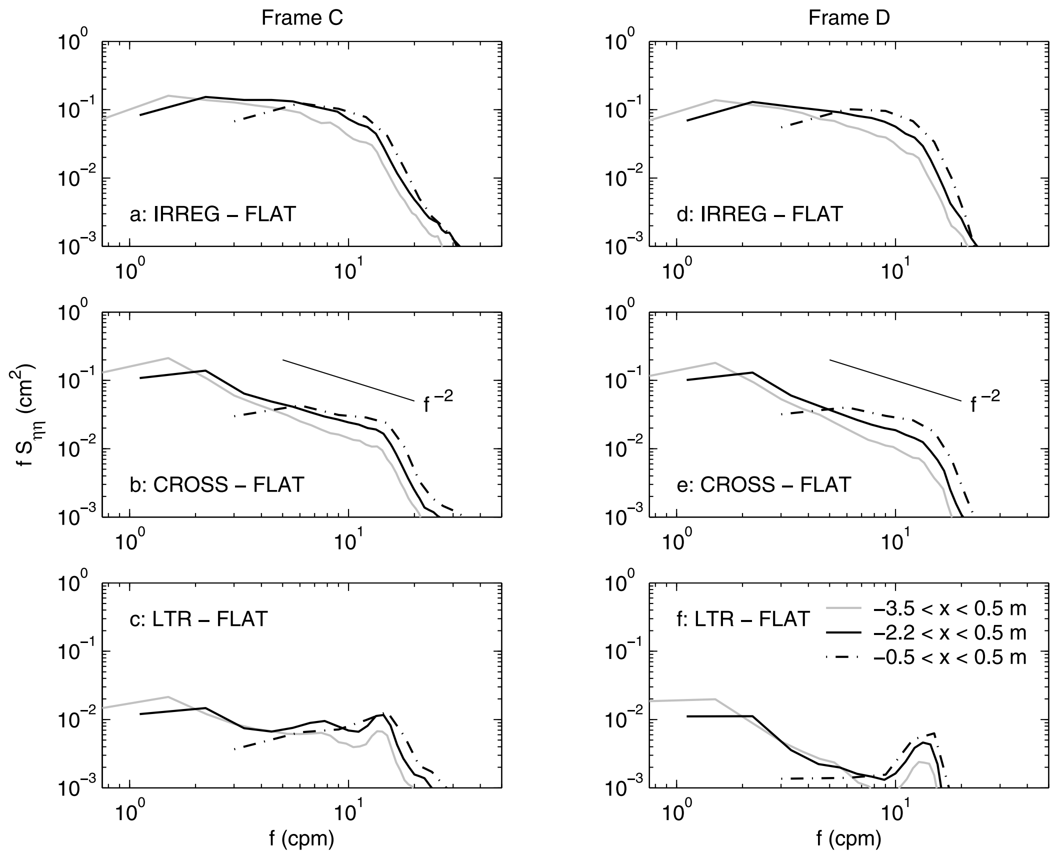

Figure 6. Variance-preserving plots of the average roughness spectra versus bed state, with the average flat bed spectrum subtracted out, for frames (left) C and (right) D: (a and d) irregular ripples; (b and e) cross ripples; and (c and f) linear transition ripples. The straight lines in Figures 6b and 6e represent $S_{\eta\eta} \propto f^{-2}$ i.e., constant steepness. Other line types are as per the legend in Figure 6f.

SandyDuck97 at the same frame locations for the same bed states. For LTRs, *Maier and Hay* [2009] obtained $\lambda_\circ = 7.6 \pm 0.06$ cm. For cross ripples, *Cheel and Hay* [2008] obtained mean wavelengths of 44 and 55 cm for the long-wavelength component at the two frames, and 9.6 to 9.8 cm for the short-wavelength component (these are the values from the radial spectra). *Hay and Mudge* [2005] obtained wavelengths of 7.7 to 20 cm for irregular ripples.

Table 3. Mean Standard Deviation of Spectrum-Based Ensemble Estimates of Ripple Wavelength, Height, and Steepness[a]

Ripple Type	N_E	λ_{oE} (cm)	η_{oE} (cm)	η_{oE}/λ_{oE}
		Frame C		
Irregular	25	26 ± 5.0	3.33 ± 0.36	0.13 ± 0.03
Cross	41	59 ± 14.9	2.34 ± 0.52	0.042 ± 0.013
LTRa	60	6.9 ± 0.24	0.98 ± 0.21	0.14 ± 0.03
LTRb	30	6.9 ± 0.21	0.34 ± 0.23	0.050 ± 0.03
		Frame D		
Irregular	25	28 ± 4	3.10 ± 0.27	0.11 ± 0.024
Cross	45	68 ± 21	2.07 ± 0.44	0.033 ± 0.011
LTRa	110	7.0 ± 0.2	0.81 ± 0.18	0.12 ± 0.025
LTRb	69	7.0 ± 0.2	0.24 ± 0.17	0.034 ± 0.02

[a] N_E is the number of ensembles. Each ensemble comprises 10 realizations with a maximum time between consecutive realizations of 2h. The LTRb estimates are corrected for the flat bed spectrum.

[22] Figure 7 shows the ripple wavelengths from Table 3 plotted against orbital excursion, both normalized by median grain size. The orbital excursions are based on the RMS wave orbital velocities and wave periods listed in Table 4, i.e., with $u_{1/3} = 2u_{rms}$ the significant wave orbital velocity

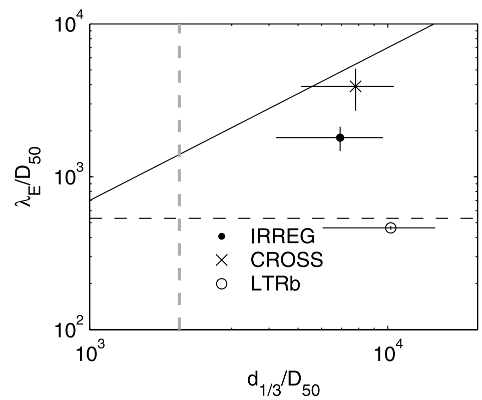

Figure 7. Ripple wavelengths versus orbital excursion, normalized by D_{50}, based on data in Table 3. Error bars indicate ±1 standard deviation.

Table 4. Summary of the Forcing Statistics[a]

	Irregular	Cross	LTR	Flat
		Frame C		
N	484	641	1078	2104
u_{rms}, m/s	0.13 ± 0.025	0.18 ± 0.023	0.24 ± 0.048	0.43 ± 0.077
$\underline{T}_p$, s	11.4 ± 2.5	9.7 ± 1.8	9.1 ± 2.3	9.8 ± 2.1
$\overline{\Psi}$	27	52	92	296
$\overline{\theta}_{2.5}$	0.13	0.23	0.39	1.09
		Frame D		
N	431	671	1575	2031
u_{rms}, m/s	0.14 ± 0.029	0.18 ± 0.032	0.27 ± 0.052	0.42 ± 0.122
$\underline{T}_p$, s	11.8 ± 2.3	10.1 ± 2.2	9.0 ± 1.9	9.3 ± 2.2
$\overline{\Psi}$	32	52	117	282
$\overline{\theta}_{2.5}$	0.14	0.23	0.48	1.06

[a] N is the number of occurrences of each bed state.

[*Thornton and Guza*, 1983], and T_p the peak wave period, the significant orbital excursion is given by

$$d_{1/3} = 2u_{1/3}/\omega, \tag{6}$$

where $\omega = 2\pi/T_p$. (Note that the values in Table 4 differ slightly from the values for the same parameters of *Hay and Mudge* [2005] due to the criteria for dealing with bed state co-occurrences being different: that is, co-occurrences of mud with either rippled or flat beds have been excluded here, and cross ripples combined with LTRs have been counted here as cross ripple occurrences, but excluded from the LTR occurrences.) Also plotted in Figure 7 are lines indicating the expected locations of particular ripple types. The solid line indicates the linear dependence of wavelength on orbital excursion expected for orbital ripples, $\lambda \sim 0.7d_{1/3}$ [*Clifton and Dingler*, 1984; *Wiberg and Harris*, 1994; *Traykovski et al.*, 1999]. The vertical dashed line represents the value of $d_{1/3}/D_{50}$ at which orbital ripples are no longer expected to occur and suborbital ripples to begin [*Clifton and Dingler*, 1984]. The solid horizontal line indicates the value of λ/D_{50} for anorbital ripples, with wavelengths characteristically independent of orbital excursion for a given grain size. Using the SandyDuck97 fan beam imagery, *Maier and Hay* [2009] have demonstrated that LTR wavelengths are closely clustered about the anorbital line, which led them to conclude that LTRs are anorbital ripples. The present pencil beam results are consistent with this conclusion. Cross ripples and irregular ripples tend to fall below the orbital ripple line, above the anorbital line, and to the right of *Clifton and Dingler*'s [1984] boundary between orbital and suborbital ripples. Thus, irregular ripples and cross ripples are suborbital-type ripples in that sense. However, it should be born in mind that cross ripples involve 2 distinct wavelengths and orientations, and the ripple crests are not orthogonal to the incident wave direction [*Cheel and Hay*, 2008]. Thus, it is unclear either how or if cross ripples should be represented in the parameter space of Figure 7.

[23] Figure 8 shows ripple steepness plotted versus the grain roughness Shields parameter,

$$\theta_{2.5} = \frac{f'_w u_{bo}^2/2}{(s-1)gD_{50}}, \tag{7}$$

where u_{bo} is the near-bed orbital velocity amplitude (set equal to $u_{1/3}$), s the sediment grain specific gravity (set equal to 2.7), g the gravitational acceleration, and f'_w the grain roughness wave friction factor (computed using Swart's friction factor formula with $2.5D_{50}$ for the roughness and $d_{1/3}/2$ for the orbital excursion amplitude [*Nielsen*, 1992, pp. 25 and 105]). Also shown in Figure 8 are the empirical steepness curves obtained by *Nielsen* [1981] using the then-available field and laboratory data. The irregular ripple and LTRb steepnesses fall close to and somewhat below *Nielsen*'s [1981] field data curve. In contrast, the cross ripple steepness lies well below this curve. That cross ripple steepness should be anomalously low relative to other ripple types may simply be indicative of their three-dimensional character and the fact that the ripple crests are not orthogonal to the incident wave direction. (Note that, on the basis of the results reported by *Cheel and Hay* [2008], the pencil beam profiles would have intersected the cross ripple crests at an angle of about 50° on average. The associated steepness correction would be a 55% increase, which does significantly affect the location of the cross ripple points in Figure 8).

[24] Now consider the LTRs. Also shown in Figure 8 is the LTR steepness reported by *Crawford and Hay* [2001], which is very close to the LTRb value obtained here. Their bed profile measurements were made using a laser-video system with millimeter resolution [*Crawford and Hay*, 1998] and are the most accurate LTR measurements of which the author is aware, so this level of agreement with the pencil beam data is encouraging.

3.4. Ripple Adjustment Times

[25] The rather abrupt changes in roughness during both storm wave growth and decay indicated in Figures 1 and 2 are pursued further here. An expanded view of the variance changes during one storm event is shown in Figure 9, to illustrate the procedure used to quantify the response times. Approximate event start and end times were determined visually, and then baseline variances immediately before and after the event, as well as the mean variance during the event, were computed. The time at the start of increasing

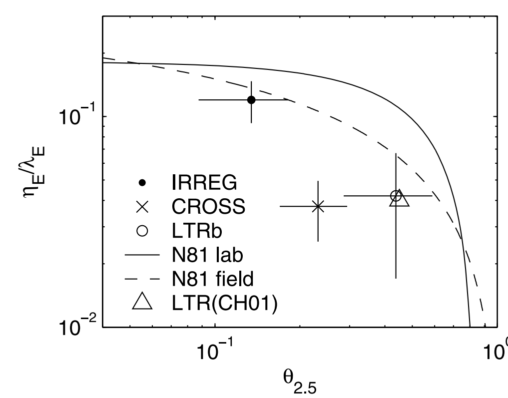

Figure 8. Ripple steepness versus grain roughness Shields parameter. The points indicated by dot, cross, and circle are from this study. CH01 is the observed LTR value from *Crawford and Hay* [2001]. The solid and dashed curves are the best fit relations to laboratory and field data, respectively, obtained by *Nielsen* [1981].

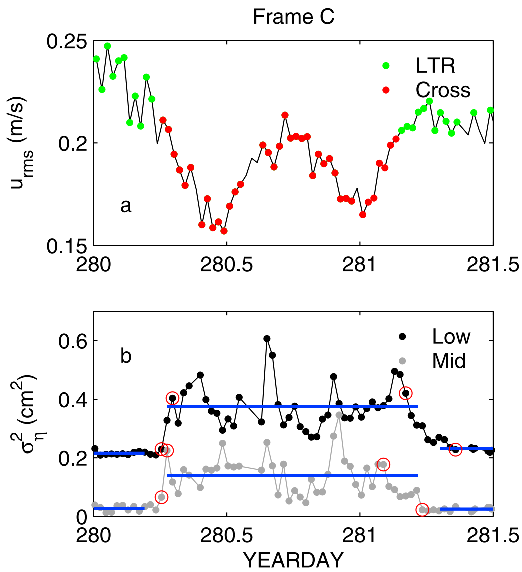

Figure 9. A single high roughness "event," showing (a) the wave forcing and bed state time series and (b) the bed elevation variance time series in the low-frequency and midfrequency bands, the former being offset by 0.2 cm^2. In Figure 9b, the solid blue lines indicate the baseline variances before and after the event and the mean variances during the event. The red circles indicate the times t_1 through t_4 on which the observed response times in Table 5 were based, as explained in the text.

roughness, t_1, was defined to coincide with the last occurrence of a variance less than or equal to the preevent baseline level. The end of increasing roughness, t_2, was defined to be the time corresponding to the first variance value greater than the mean. A like procedure was used for t_3 and t_4, which correspond to the start and end of roughness decay. These times, which are indicated for the event in Figure 9 by the open red circles, yield estimates of the ripple response time, T_R: that is, $T_{Rr} = t_2 - t_1$ is the response time during rising roughness (and decaying wave energy), while $T_{Rf} = t_4 - t_3$ is the response time during falling roughness (and increasing wave energy). The observed response times for 7 events at each of the two frames are listed in Table 5 and range from 0.5 h to 18 h, with mean values of 2 to 5 h. Surprisingly perhaps, there is no consistent difference (in the mean) between the response times for rising and falling roughness, emphasizing the point raised earlier with respect to the time series in Figures 1 and 2 that the roughness response times are similar during both wave energy growth (falling roughness) and decay (growing roughness).

[26] The sequence of bed states during the roughness response time intervals are also indicated in Table 5. During increasing roughness the transition is in most cases from LTRs to cross ripples (i.e., LX), and similarly from cross ripples to LTRs (i.e., XL) during decreasing roughness. There are exceptions, including instances where the sequence is from irregular ripples through LTRs to flat bed, with no observed cross ripple occurrence. These instances correspond to very rapid increases in wave energy at the onset of storm events (compare the ILF times in Table 5 to Figure 1a).

[27] A theoretical estimate of ripple adjustment time is given by the ratio of the volume of sediment in the ripple to the volume rate of sediment transport, namely,

$$T_R = (1 - n)\frac{\eta_o \lambda_o}{2Q_b}, \tag{8}$$

Table 5. Observed Bed Elevation Variance Response Times T_R[a]

Time Interval (year day)	T_{Rr} (h) Low	T_{Rr} (h) Middle		T_{Rf} (h) Low	T_{Rf} (h) Middle	Rise Sequence	Fall Sequence
				Frame C			
248.6–251	3.7	3.7		5	3.5	LX	IXL
259.6–264.5[b]				7.7	1.2		IX
268.8–270.6	1.8	2.7		1	10	FX	XL
275–280	4.5	18		2.5	9	LX	IL
280–281.5	1	0.5		4.5	3.5	LX	XL
296.8–298.4[c]	4.5	3			4	LX	ILF
301.9–304.7	1.7	3		1.7	3	LX	XL
Mean T_R (h)	2.9	5.1	3.7	4.9			
				Frame D			
248.6–250.8	5.8	1.3		1.5	0.5	LX	XL
259.6–264.5[b]				1.3	0.7		ILF
268.8–270.6	2.3	1.7	5.5		5.5	LX	LF
275.5–279.8				4	6	LX	XL
280–281.5	4.5	2		4	4	LX	XL
296.8–298.2	1	2.5		2.5	6		XL
302–304.6	1.3	4.2		1.3	2	LX	XL
Mean T_R (h)	3.0	2.3		2.9	3.5		

[a] T_{Rr} and T_{Rf} denote the response times during rising and falling roughness at the beginning and end, respectively, of each roughness "event". "Low" and "Middle" indicate the low-frequency and midfrequency bands (Table 1). The bed state sequences are indicated via the letter designations: I, irregular ripples; X, cross ripples; L, linear transition ripples; F, flat bed.

[b] Missing roughness data on rise.

[c] Megaripple at large x on fall contaminates low band.

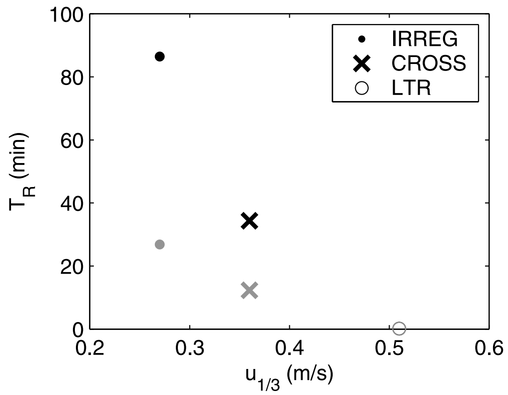

Figure 10. Response times computed using equation (8) for the different rippled bed states. The grey points were obtained using Q_b determined from equation (9) assuming $u_{1/3}$ constant; the dots were obtained using $Q_b = \overline{Q}_b$, the time-averaged half-cycle transport assuming sinusoidal waves, using the "standard" parameter values in each case.

where n is the sediment porosity and Q_b is the bed load transport during a half cycle, which can be estimated using the bed load formula proposed by *Meyer-Peter and Müller* [1948] [see also *Nielsen*, 1992, p. 120]:

$$Q_b = \frac{A}{(s-1)g}\left(\frac{\tau_b - \tau_c}{\rho}\right)^{3/2}, \tag{9}$$

where A is a constant, τ_b is the bottom stress, and τ_c is the critical stress for grain movement. Equation (9) is referred to hereafter as the MPM relation.

[28] *Traykovski* [2007] has invoked equation (8) and a similar MPM relation in his model of the temporal evolution of orbital-scale ripple wavelengths during storms. *Maier and Hay* [2009] applied equations (8) and (9) to the adjustment of LTR orientation to changing wave direction. *Maier and Hay* [2009] also compared adjustment times so predicted to the available laboratory measurements, finding agreement (within a factor of 2 or 3), at least for mobility numbers greater than 25. (The mobility number, $\Psi = 2\theta_{2.5}/f'_w$.) Note that *Maier and Hay* [2009] dropped τ_c from the bed load equation, since $\theta_{2.5} \gg \theta_c$ for LTRs. A typical value of the critical Shields parameter in sandy sediments is 0.05 [*Nielsen*, 1992]. Referring to Table 4, it is clear that $\theta_{2.5}$ cannot be taken to be much greater than θ_c for the irregular and cross-ripple bed states.

[29] The predicted adjustment times are plotted in Figure 10. These estimates were obtained using equations (8) and (9) with the values of the forcing parameters in Table 4, A = 10, s = 2.7, and the ripple heights and wavelengths from Table 3. Two sets of predictions are plotted for each bed state: one, the grey points, with Q_b based on $u_{1/3}$ being constant throughout a half cycle; the second, the black points, with Q_b time dependent and integrated to obtain the half-cycle average transport, $\overline{Q}_b$. (The half-cycle average transport was computed using $\tau(t) = \rho f'_w u_b(t)^2/2$; $U_b(\mathrm{t}) = u_{1/3} \sin 2\pi t/T_p$, and $\overline{Q}_b = 2\int_0^{Tp/2} Q_b(t)\mathrm{d}t/T_p$.)

[30] The predicted response times for LTRs are very short, 4 to 9 s, consistent with the values given by *Maier and Hay* [2009], and with the observations reported by *Dingler and Inman* [1977] and others of anorbital ripples being created and destroyed on wave period timescales. In contrast, the predicted values of T_R for the other rippled bed states are much longer, and approach but are still significantly less than the observed mean values of T_R listed in Table 5: i.e., a typical value of T_R for an LX or XL transition is about 3 h, whereas the prediction based on equation (8) using $\overline{Q}_b$ is at most 1 h, a factor of 3 shorter.

[31] Thus, the predicted adjustment times are less than those observed, especially considering that for most of the observed instances the principal transition involves cross ripples either developing from LTRs, or deteriorating in favor of LTRs. One possible explanation, discussed by *Maier and Hay* [2009] with respect to the delayed reorientation of LTRs in response to rapid changes in wave direction, is sediment bypassing (including bypassing as suspended load). The bypassing argument put forward by *Maier and Hay* [2009] for ripple orientation adjustment could in principle also apply to the temporal adjustment of bed state to changing forcing conditions being investigated here: that is, only a fraction of Q_b contributes to the transport divergence involved in adjusting to the new bed state. However, another possibility is that equation (9) overestimates Q_b. *Ribberink* [1998] obtained best fit values of A = 11, and 1.65 instead of 1.5 for the exponent in equation (9), using D_{50} instead of $2D_{50}$ for the roughness in Swart's formula. *Ribberink* [1998] also used the grain-size-dependent critical Shields parameter proposed by *van Rijn* [1993] which, for D_{50} = 150 μm, would be 0.707. Using these values to compute $\overline{Q}_b$ does lead to larger estimates of T_R: by factors of 6.0, 2.5, and 1.7 for irregular ripples, cross ripples, and LTRs, respectively. The factor of 1.7 change for LTRs is not enough to alter the conclusions drawn by *Maier and Hay* [2009], since they needed orders of magnitude longer predicted response times to reconcile the observed time lag between LTR orientation adjustment and rapid changes in wave direction. However, the factor of 2.5 change for cross ripples would be enough to bring the predicted roughness adjustment times into line with the observed times presented here.

4. Discussion

4.1. Bed State Repeatability and Predictability

[32] *Gallagher et al.* [2003] have also reported observations of (geometric) bed roughness during SandyDuck97, measured using sonar altimeters mounted on a mobile platform, from which RMS roughness was mapped throughout the experiment domain. As mentioned previously, the bed elevation spectra were red, as is the case here. Two additional observations by *Gallagher et al.* [2003] are of particular relevance. (1) The mobility number was found *not* to be a good predictor bed state (defined by *Gallagher et al.* [2003] as large ripples, small ripples or flat bed on the basis of the measured RMS roughness) for $30 \lesssim \Psi \lesssim 150$. (2) The spatial distribution of *large ripple roughness* tended to be patchy, especially at distances beyond the crest of the inner bar. In *apparent* contrast with observation 1, mobility number and wave energy being equivalent for a given grain size, bed state at the two rotary sonar locations (which were located beyond the crest of the inner bar) was a highly repeatable function of wave energy [*Hay and Mudge*, 2005],

and the results presented here indicate a consistent decrease in RMS roughness with increasing wave energy and mobility number (Tables 2 and 4) for $30 \lessapprox \Psi \lessapprox 300$.

[33] Because the elevation spectra are red, RMS roughness estimates will be dominated by the lowest spatial frequencies in the spectral band included in the estimate. The roughnesses computed by *Gallagher et al.* [2003] included frequencies down to 0.1 cpm, and their roughness variability was therefore dominated by the presence/absence of megaripples [see also *Gallagher et al.*, 2005]. Here not only is the lowest resolved frequency nearly an order of magnitude higher (0.7 cpm), but also megaripple occurrences have been excluded from the present analysis, for the following reasons. The rotary fan beam sonar data indicate that meter-scale lunate forms sometimes persisted for 24 h or more while migrating across the 10 m diameter field of view of the sonar. Thus, these features can be long-lived relative to the timescales of changes in the forcing and were therefore likely to be out of equilibrium with the forcing conditions at some time(s) during their life history. Frequently only one megaripple was present in the sonar field of view, indicating that the intermegaripple spacing was O(10 m) or greater. Thus, even the rotary fan beam data do not reliably indicate megaripple presence: the 10 m field of view is too restricted. Furthermore, such isolated megaripples within the fan beam field of view were often not located on the cross-shore line swept by the pencil beam. Figure 1 provides several instances: e.g., on year days 239–241 a megaripple was present in the fan beam imagery for more than 48 h but there is no corresponding signal in the roughness time series from the pencil beam profiles. Thus the pencil beam data do not provide representative values for the time-varying relief of these features during the 10 forcing events, and in consequence megaripples cannot be included in the present analysis of changes in the ensemble-averaged roughness over the course of the bed state storm cycle.

[34] A significant contributor to the roughness variability observed by *Gallagher et al.* [2003], and the consequent poor correlation between RMS roughness and mobility number in their results, was the patchy nature of the megaripple spatial distribution over the O(10^4 m^2) mapped area. *Gallagher et al.* [2003] suggested patchiness in the spatial distribution of bed sediment grain size as one potential cause. The question then arises as to whether there were significant grain size variations within the fields of view of the rotary sonars at the two locations involved here. In their study of LTRs at these same frame locations, *Maier and Hay* [2009] found that the wavelength of these anorbital ripples was constant within ±10% over the full 2.5 months of the data record, and inferred that the grain size of the surficial bed sediments was also constant to within ±10%. Note that, after flat bed, LTRs were the most frequently observed bed state at the frame C and D locations [*Hay and Mudge*, 2005].

[35] Thus, the differences between the present study of geometric roughness during SandyDuck97 and that of *Gallagher et al.* [2003] can be ascribed to differences in the spatial frequency band over which RMS roughness was determined, differences in the definition of bed state, the exclusion of megaripples from the present analysis, and the likelihood that megaripples are at times out of equilibrium with the forcing. Returning then to the statement in the introduction regarding bed state predictability, it can now be restated on the basis of the results presented here and by *Hay and Mudge* [2005] that the repeatability of the bed state storm cycle provides grounds for optimism that, given the grain size, both the spatial pattern and geometric roughness characteristic of different bed states in nearshore sands could one day be predictable from first principles.

4.2. Ripple Response Times

[36] A number of recent laboratory investigations have led to empirical relationships between ripple adjustment time and either the mobility number [*Voropayev et al.*, 1999; *Doucette and O'Donoghue*, 2006; *Soulsby and Whitehouse*, 2005] or the Shields parameter [*Davis et al.*, 2004; *Smith and Sleath*, 2005]. These formulae were compared to equation (8) by *Maier and Hay* [2009], using the original laboratory data where appropriate. *Maier and Hay* [2009] concluded that, for the high mobility number range of interest, predicted response times based on equation (8) were in satisfactory agreement with the laboratory results.

[37] The present results provide support for equation (8) at low mobility numbers as well. This extended range of support comes, however, with the caveat that the predicted response times at low values of Ψ are sensitive to the details: that is, to the values of the parameters used in the bed load transport equation. Specifically, for irregular ripples, the predicted value of T_R increased by a factor 6 when *Ribberink*'s [1998] formulation for Q_b was used instead of the more standard form, i.e., 1.65 versus 1.5 for the stress exponent; D_{50} versus $2D_{50}$ for the physical bed roughness in Swart's relation for f_w; and τ_c = 0.707 instead of 0.05. Each of the changes made separately makes a comparable contribution to the increase, i.e., 41%, 54%, and 61%, respectively (the greater than 100% total implying compensation among the three parameters).

4.3. Comparison to Other Measurements of Geometric Ripple Roughness

[38] As mentioned previously, *Crawford and Hay* [2001] reported high-precision measurements of LTR elevation profiles obtained with a laser-video system. The reported values of LTR wavelength, height, and steepness (in 174 μm median diameter sand) were 8.5 cm, 3 mm, and 0.04, respectively. Previously, *Dingler* [1974] had observed anorbital wavelengths of 7 to 8 cm, heights of 3 to 5 mm, and steepnesses between 0.04 and 0.07 in 130 to 170 μm median diameter sands. Thus, the results from these two studies of anorbital ripples are comparable to the values reported here for linear transition ripples.

[39] *Hanes et al.* [2001] also reported ripple heights and wavelengths during SandyDuck97, but farther offshore in ~4 m water depth. The median grain diameter of the sand at their location was 157 μm. Ripple geometry measurements were made with a 2.5 m long, cross-shore oriented linear array of acoustic transducers. Ripples were broadly characterized as short-wavelength ripples (SWRs, $\lambda_\circ \leq 25$ cm) or long-wavelength ripples (LWRs, $\lambda_\circ \leq 35$ cm). As information on ripple pattern was lacking, their SWRs likely included LTRs, the short-wavelength component of cross ripples, and possibly irregular ripples. *Hanes et al.* [2001] also presented measurements made from the FRF pier in 1995 and 1996. Of the SWR heights measured from the pier

(in sand with median diameters below 200 μm), many were between 2 and 4 mm (e.g., 10 of 25 in the 1996 data), similar to the values reported here (Table 3).

[40] *Hanes et al.* [2001, p. 22,591] state that LWRs "are still particularly perplexing because of their low slopes." Restricting attention to the 55 instances in their Table 6 for which $\lambda \leq 1.33$ m (the longest resolved wavelength here), the mean observed LWR height and steepness were 1.8 ± 1.1 cm and 0.02 ± 0.01. The corresponding values of T_p, D_{50}, and $d_{1/3}$ give $\overline{\theta}_{2.5} = 0.62$. However, the $\theta_{2.5}$ values are broadly distributed, from a minimum of 0.029 to a maximum of 3.0, and 35% are within 2 standard deviations of 0.23, the mean for cross ripples (the standard deviation referred to here is 0.06, the value for cross ripples given by *Hay and Mudge* [2005]). Thus, a substantial number of the LWR occurrences reported by *Hanes et al.* [2001] could have been cross ripples, which would potentially resolve the low-slope question since cross ripple steepnesses are shown here to be anomalously low (Figure 8).

4.4. Linear Transition Ripples and Clifton's Spatial Progression

[41] Except for flat bed, linear transition ripples represent the most frequent bed state in ~3 m water depth during SandyDuck97. *Clifton* [1976] did not include this ripple type in his progression, although the occurrence of these anorbital ripples is indicated by *Clifton et al.* [1971], the observational paper upon which his spatial progression was based. Specifically, *Clifton et al.* [1971] state that "under certain wave conditions, small sand ripples may cover the surface of the outer planar facies" (located immediately shoreward of the lunate megaripple zone) which "are very regular and have a very long crest length compared to their wavelength (about 10 cm) and amplitude (less than 1 cm)." Based on this description, these ripples were undoubtedly the linear transition ripples identified in the SandyDuck97 data and discussed in detail by *Maier and Hay* [2009]. *Clifton et al.* [1971] go on to state that these ripples also co-occurred with lunate megaripples, provided the waves were not too energetic. Thus, it can be inferred that, in the spatial progression put forward by *Clifton* [1976], linear transition ripples would constitute a rippled bed state at wave energies immediately below the transition to flat bed, just as they do in the temporal progression.

[42] The *Maier and Hay* [2009] paper was based on the fan beam sonar imagery and therefore on LTR spatial pattern and wavelength. The present paper provides the corresponding information on LTR heights during SandyDuck. As discussed by *Maier and Hay* [2009], the fact that LTRs are observed in the field but not in recent large-scale laboratory experiments [e.g., *O'Donoghue et al.*, 2006] has raised the question as to why this should be so. One possibility, suggested by *Pedocchi and Garcia* [2009], is that LTRs occur only in fine-grained sand at low particle Reynolds numbers which tend to lie outside the parameter range of the large-scale laboratory experiments to date.

5. Summary and Conclusions

[43] The geometric roughness associated with different bed states occurring in nearshore sands has been determined from bed elevation profiles measured with rotary pencil beam sonars over a ~2.5 month period. This period encompassed 10 wave forcing events sufficiently energetic to flatten the bed, resulting in 10 associated realizations of the bed state storm cycle, i.e., the sequence during wave energy growth from irregular ripples initially through cross ripples and linear transition ripples to flat bed, followed by the reverse sequence during wave energy decay. Roughness is estimated both spectrally and by band-pass filtering. The spectral representation of roughness is used to obtain ensemble-averaged wavelengths, heights, and steepnesses for irregular, cross, and linear transition ripples. The band-passed method yields roughness time series, which are used to estimate the bed state response times. These observed response times are compared to predictions based on the spectral estimates of ripple height and wavelength and on the bed load transport rates predicted using stress-based semiempirical formulae of the MPM type. The main conclusions of the work are outlined below.

[44] 1. The roughness time series are coherent across the 3 spatial frequency bands, and between the two instrument frame locations within a given band.

[45] 2. The observed wavelengths of the different ripple types, plotted in λ/D_{50} versus $d_{1/3}/D_{50}$ parameter space, indicate that irregular and cross ripples are suborbital ripple types and that linear transition ripples are anorbital.

[46] 3. The observed steepnesses of irregular ripples and linear transition ripples fall slightly below the steepness vs Shields parameter curve obtained by *Nielsen* [1981] for field data. Relative to these two ripple types and the *Nielsen* [1981] curve, the observations indicate that cross ripple steepnesses are anomalously low, providing a possible explanation for the otherwise "perplexing" low-steepness long-wavelength ripples reported by *Hanes et al.* [2001].

[47] 4. Changes in roughness associated with wave-forcing events were often quite abrupt, especially in the low-frequency and midfrequency bands. The observed timescale associated with the abrupt roughness changes was about 3 h on average, and essentially the same on average for both decreasing and increasing roughness (i.e., both during periods of growing and decaying wave energy).

[48] 5. The bed state transitions associated with the abrupt roughness changes were most frequently from cross ripples to linear transition ripples during wave energy growth, and from linear transition ripples to cross ripples during wave energy decay.

[49] 6. Predicted roughness response times, based on the volume of sand in the ripple and the bed load transport rate Q_b computed via a formula of the MPM type, are in quite good agreement with the observations when the parameter values obtained by *Ribberink* [1998] are used. The more standard values for grain roughness, critical shear stress, and the exponent in the MPM formula [e.g., *Nielsen*, 1992] yield much shorter response times.

[50] 7. *Ribberink*'s [1998] values are based on an analysis of bed load transport measurements in oscillatory flow (carried out in 3 different flow tunnel facilities) and is the most extensive such analysis of which I am aware, which is why I have used them here. Importantly, I have not arbitrarily sought out values in the literature which would give improved agreement with the observations.

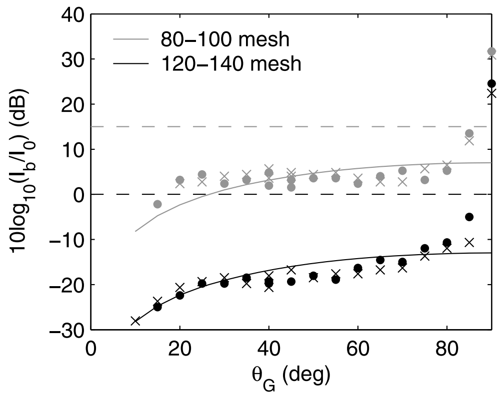

Figure A1. Backscattered intensity as a function of grazing angle, θ_G, from the sand-water interface for two sieved sand fractions, 80 to 100 mesh ($D_{50} \sim 165\ \mu m$) and 120 to 140 mesh ($D_{50} \sim 115\ \mu m$), at 1.0 to 1.1 MHz. The data are taken from *Nolle et al.* [1963, Figures 17 and 18]. The dashed lines indicate 0 dB. The 80 to 100 mesh data are offset by 15 dB. The solid lines indicate the predicted profiles for Lambertian scattering, using Lambert parameter values ($10 \log_{10} \mu$) of −8 and −13 dB for the $D_{50} \sim 165\ \mu m$ and $D_{50} \sim 115\ \mu m$ data, respectively. These values are comparable to those reported by *Greenlaw et al.* [2004] for field measurements of backscatter from sandy sediments at MHz frequencies.

[51] 8. It is also important to note that the differences between the standard parameter values in the MPM formula and those obtained by *Ribberink* [1998], taken separately, each result in a ~50% contribution to the increase. Of the three parameters, the predictions are most sensitive to the value of the critical stress. Specifically, of the factor of 6 increase in the predicted adjustment time for irregular ripples, 61% (or more than a factor of 3), could be accounted for by the use of a grain-size-dependent critical shear stress alone. This dependence on grain size is recognized in the literature [*van Rijn*, 1993; *Soulsby and Whitehouse*, 1997; *van der Veen et al.*, 2006]. The value I have used, 0.071, is based on the work of *van Rijn* [1993] to be consistent with *Ribberink* [1998] and, being larger than the "standard" value of 0.05, leads to longer predicted response times.

[52] 9. The fact that geometric roughness adjustment times from the present data set can, *on average*, be adequately accounted for on the basis of bed load transport alone indicates that sediment bypassing and suspended sediment transport were not major contributors to roughness adjustment. This agreement between the observations and predictions further indicates that, *on average*, geometric roughness adjustment was in quasi-equilibrium with bed load transport divergence on the spatial scales of the bed forms. *Maier and Hay* [2009] came to a similar conclusion in their investigation of ripple crest orientation adjustment: that is, crest orientation usually kept pace with the changing direction of the incoming waves, implying quasi-equilibrium with the forcing. However, when the changes in the forcing direction were very abrupt, ripple orientation was found to lag the change in the forcing by O(1 h). *Maier and Hay* [2009] suggested sediment bypassing as a possible cause, i.e., that the horizontal divergence of the transport, both bed load and suspended load, was (had to be) distributed over other spatial scales to accommodate the ripple crest reorientation, leading to the delayed response. By extension, bed roughness at the ripple scale may also not be able to adjust rapidly enough to remain in quasi-equilibrium with the forcing when changes in the wave energy are sufficiently abrupt, and one could speculate that in such cases bypassing would play an important role.

[53] 10. Synthetic elevation profiles and spectra are obtained using a model of acoustic backscatter from a rippled sand-water interface assuming that backscatter from a sandy seabed is Lambertian, and the same deployment geometry and sonar operating parameters as in the field experiment. The comparisons to available measurements at MHz frequencies indicate that this assumption is reasonable for angles of incidence $\gtrsim 10°$. The model supports the use of intensity-weighted estimator of range to the seabed, and successfully reproduces the observed dependence of spectral roll-off on the spatial interval over which the spectra are determined.

Appendix A: Simulated Ripple Profiles and Elevation Spectra

[54] As mentioned previously, the steeper roll-off at high spatial frequencies for spectra computed over wider x intervals (see Figure 6) cannot be the result simply of smoothing by the finite width of the sonar beam. To investigate this effect, a model is developed below assuming that the backscattered intensity from the sand-water interface, I_b, is Lambertian at MHz frequencies, i.e., that I_b is proportional to $I_\circ \cos^2 \theta$, where $I_\circ$ is the incident intensity at the bed and θ is the angle of incidence.

[55] Lambertian scattering of sound by a rippled sandy seafloor has been invoked previously by *Tang et al.* [2009], who developed an algorithm for inverting side scan sonar amplitudes at 300 kHz to obtain estimates of ripple height. The validity of the Lambertian approximation for acoustic backscatter from the sand-water interface at MHz frequencies is examined in Figure A1. Figure A1 shows the results of laboratory experiments carried out by *Nolle et al.* [1963] for nominally flat sand-water interfaces as a function of grazing angle, θ_G (= 90° − θ), and are the only such laboratory experiments in the MHz frequency range of which the author is aware. *Nolle et al.* [1963] did not compare their measurements to Lambert's law, however, which is given by

$$I_b = \mu I_0 \cos^2 \theta, \qquad \text{(A1)}$$

μ being the Lambert parameter, so curves based on this relation using a best fit by eye are plotted in Figure A1. For $\theta \gtrsim 10°$, the data and equation (10) are in reasonably good agreement. In addition, as indicated in the Figure A1 caption, the values of the Lambert parameter are comparable to those determined by *Greenlaw et al.* [2004] from field measurements of backscatter at MHz frequencies and large angles of incidence. The departures from the Lambertian

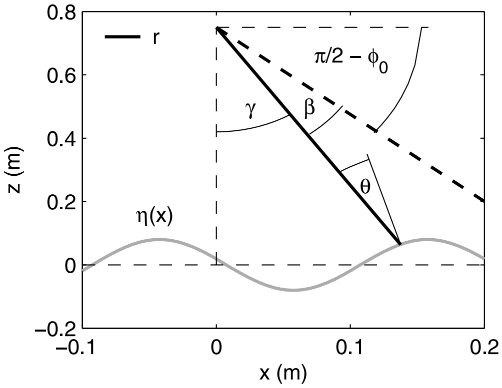

Figure A2. Sketch of the geometry used in the simulations. The transducer is at $x = 0$, $z = 0.75$ m. The thick dashed line represents the acoustic axis, at training angle $\phi_\circ = \gamma + \beta$ from the vertical. The thick solid black line represents the ray of length r at angle β from the acoustic axis, and intersecting the ripple profile at θ, the angle of incidence.

prediction near normal incidence in Figure A1 are due to specular reflection [*Nolle et al.*, 1963]. Because the rotary sonar data tend to be clipped at near-normal incidence, this specular peak is not included in the model.

[56] The geometry used in the simulations is shown in A2. The radial distance from the transducer to any point on the ripple profile is

$$r = \left([r_\circ - \eta(x)]^2 + x^2 \right)^{1/2}, \tag{A2}$$

where $r_\circ$ is the vertical distance to the mean bed level, and

$$\eta(x) = a_\circ \sin(2\pi x/\lambda_\circ + \vartheta) \tag{A3}$$

is the ripple profile, ϑ being an arbitrary phase. The angle of inclination of r with respect to the vertical is denoted by γ, and given by

$$\tan\gamma(x) = \frac{x}{r_\circ - \eta(x)}. \tag{A4}$$

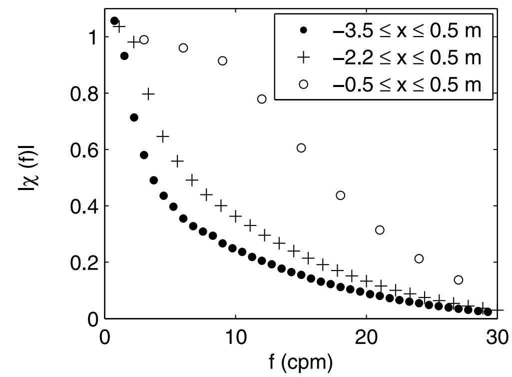

Figure A4. Simulated transfer function magnitudes. The symbols indicate the results for the different x intervals over which bed elevation spectra were computed (see Table 1); $\beta_\circ = 1°$. a_0 = constant.

The angle of the acoustic axis relative the vertical is $\phi_\circ$. The transducer beam pattern is represented by that for a uniform circular piston [*Clay and Medwin*, 1977]:

$$D = \frac{2J_1(kb_\circ \sin\beta)}{kb_\circ \sin\beta}, \tag{A5}$$

where D is the directivity, k is the acoustic wave number, $b_\circ$ is the transducer radius, and β is the angle relative to the acoustic axis.

[57] Denoting each discrete value of x by the index i, the backscattered intensity from the rippled bed at position x_i, relative to that at $x = 0$, is

$$I_{bi} = \left[\frac{r_\circ D(\beta_i)}{r_i}\right]^4 \cos^2\theta_i, \tag{A6}$$

where $\beta_i = \gamma_i - \phi_\circ$ (Figure A2). To account for contributions from the sidelobes in the transducer beam pattern, the

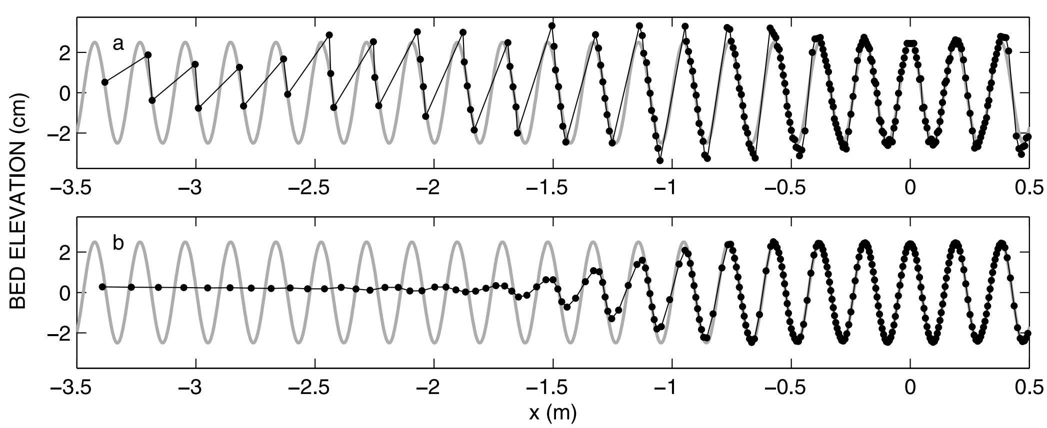

Figure A3. Simulated bed elevation profiles, indicated by the black dots, obtained assuming Lambertian backscatter from the sinusoidal profile indicated by the solid grey line, for (a) η' and (b) $\hat{\eta}$. The simulation is for the long x interval ($-3.5 \le x \le 0.5$ m, Table 1), with $\eta_\circ = 5$ cm, $\lambda_\circ = 20$ cm, and $\beta_\circ = 1°$.

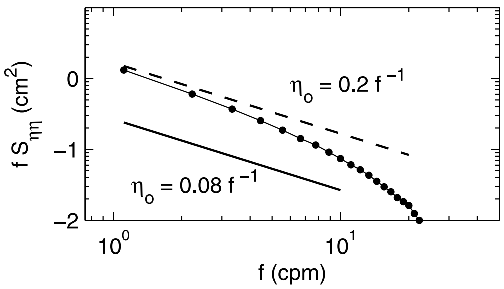

Figure A5. Model-predicted roughness spectrum, in variance-preserving form, for a constant steepness input spectrum representing orbital-scale ripples, i.e. $\eta_\circ = 0.2\lambda_\circ$, where $\eta_\circ = 2a_\circ$ (the dashed line). The points were computed at the same spatial frequencies as the observed spectra for the interval $-2.2 \leq x \leq 0.5$ m. The solid line represents an input spectrum with a lower steepness, 0.08. Compare to the observed spectra in Figure 6.

returns from all values of x such that $|\beta(x)| \leq 10\beta_\circ$ were computed. Then the corresponding intensities were summed within each range bin, giving

$$I_{bj} = \sum_i I_{bi}. \tag{A7}$$

The summation is over those values of i satisfying $|r_i - r_j| \leq c\tau/2$, i.e., within each range bin (τ is the duration of the transmit pulse, c the speed of sound in water). Equation (A7) yields a profile of backscatter intensity as a function of range at a given value of the transducer training angle, $\phi_\circ$. The range to the bottom was determined using both the intensity-weighted average range, given by

$$\hat{r}_b(\phi_\circ) = \frac{\sum_j r_{bj} I_{bj}}{\sum_j I_{bj}}, \tag{A8}$$

and the range to the maximum value of I_{bj}, denoted by r_b' ($\phi_\circ$). The simulated bed elevation profiles are given by

$$\hat{\eta}(\phi_\circ) = r_\circ - \hat{r}_b(\phi_\circ)\cos\phi_\circ, \tag{A9}$$

and

$$\hat{x}(\phi_\circ) = \hat{r}_b(\phi_\circ)\sin\phi_\circ. \tag{A10}$$

The elevation profiles corresponding to the range to maximum backscatter intensity are obtained by replacing $\hat{r}_b$ with r_b' in equations (A8) and (A9).

[58] To mimic the actual experimental conditions, the same transducer height (75 cm), transmit pulse duration (10 μs), acoustic frequency (2.25 MHz), and angular step size (0.45°) were used in the simulations. According to the manufacturer, the full (half power) beam width of the transducer is 0.9°, corresponding to $\beta_\circ = 0.45°$. The simulations were carried out for values of $\beta_\circ$ ranging from 0.5° to 1.5°, the larger values to represent the effect of clipping.

[59] Simulated $\hat{\eta}(x)$ and $\eta'(x)$ profiles for $a_\circ = 1$ cm, $\lambda_\circ = 10$ cm (i.e., values comparable to LTRs) and $\beta_\circ = 1°$ are shown in Figure A3. The profile based on maximum backscatter intensity exhibits sharp discontinuities, the result of shadowing of the ripple troughs by the adjacent ripple crests. These discontinuities are smoothed out in the $\hat{\eta}$ profile and, usefully, returns near-zero variance over this outer, shadow dominated region. For $|x| \lesssim 1$ m, $\hat{\eta}$ is in good agreement with the input bed profile, whereas relatively poor agreement is indicated when the bottom is identified with maximum backscatter intensity, particularly for $0.5 \lesssim |x| \lesssim 1$ m.

[60] The model transfer function is given by $\chi(f) = 2\sigma_\eta^2(f)/a_0^2(f)$, where $\sigma_\eta^2(f)$ is the variance of the model output after resampling at a constant interval in x, for a sinusoidal input ripple with amplitude a_0. Transfer functions are usually computed assuming a constant amplitude input. This does not make physical sense in the present application, however, as constant ripple amplitude implies that ripple steepness would increase indefinitely with increasing spatial frequency. Thus, the transfer function was computed assuming constant ripple steepness, and the resulting values are shown in Figure A4 for $\beta_\circ = 1°$ and each of the three x intervals. As Figure A4 demonstrates, the model successfully reproduces the tendency for the spectra computed over wider x intervals to roll-off more steeply with increasing frequency. The physical reason for the effect can now be identified with the fact that larger values of $|x|$ make little contribution to the variance, as noted previously with respect to Figure A3b.

[61] Simulated spectra for constant steepness ripples are plotted in variance preserving form in Figure A5. Visual comparison of Figure A5 with Figures 6b and 6e indicates that the midfrequency sections of the cross ripple spectra are reasonably consistent with the steepness being constant, the intercepts with the y axis indicating steepnesses closer to 0.1 than 0.2. The approximately constant steepness section of the irregular ripple spectra (Figures 6a and 6d) spans a narrower range of spatial frequencies.

[62] **Acknowledgments.** The author would like to thank Bill Birkemeier and the FRF staff, as well as colleagues, staff, and students at Dalhousie and Memorial Universities, for their assistance in making the field measurements. D. J. Tang was the stimulus for the backscatter model. This research was funded by the Coastal Geosciences Program of the U.S. Office of Naval Research and the Natural Sciences and Engineering Research Council of Canada.

References

Alcinov, T. (2009), Oblique long wavelength ripples in the nearshore, M.Sc. thesis, Dalhousie Univ., Halifax, Nova Scotia, Canada.

Birkemeier, W. A., H. C. Miller, S. D. Wilhelm, A. E. DeWall, and C. S. Gorbics (1985) A user's guide to the Coastal Engineering Center's (CERC's) Field Research Facility, *Tech. Rep. CERC-85-1*, 137 pp., Coastal Eng. Res. Cent., U.S. Army Corps of Eng., Vicksburg, Miss.

Cheel, R. A., and A. E. Hay (2008), Cross ripple patterns and wave directional spectra, *J. Geophys. Res.*, *113*, C10009, doi:10.1029/2008JC004734.

Clay, C. S., and H. Medwin (1977), *Acoustical Oceanography: Principles and Applications*, 544 pp., John Wiley, New York.

Clifton, H. E. (1976), Wave-formed sedimentary structures—A conceptual model, in *Beach and Nearshore Sedimentation*, edited by R. A. Davis Jr. and R. L. Ethington, *Spec. Publ. SEPM Soc. Sediment. Geol.*, *24*, 126–148.

Clifton, H. E., and J. R. Dingler (1984), Wave-formed structures and paleoenvironmental reconstruction, *Mar. Geol.*, *60*, 165–198, doi:10.1016/0025-3227(84)90149-X.

Clifton, H. E., R. E. Hunter, and R. L. Phillips (1971), Depositional structures and processes in the non-barred high-energy nearshore, *J. Sediment. Petrol.*, *41*(3), 651–670.

Crawford, A. M., and A. E. Hay (1998), A simple system for laser-illuminated video imaging of sediment suspension and bed topography, *IEEE J. Oceanic Eng.*, *23*(1), 12–19, doi:10.1109/48.659445.

Crawford, A. M., and A. E. Hay (2001), Linear transition ripple migration and wave orbital velocity skewness: Observations, *J. Geophys. Res.*, *106*(C7), 14,113–14,128, doi:10.1029/2000JC000612.

Davis, J. P., D. J. Walker, M. Townsend, and I. R. Young (2004), Wave-formed sediment ripples: Transient analysis of ripple spectral development, *J. Geophys. Res.*, *109*, C07020, doi:10.1029/2004JC002307.
Dingler, J. R. (1974), Wave formed ripples in nearshore sands, Ph.D. thesis, Univ. of Calif., San Diego.
Dingler, J. R., and D. L. Inman (1977), Wave-formed ripples in nearshore sands, paper presented at 15th Coastal Engineering Conference, Am. Soc. of Civ. Eng., New York.
Doucette, J. S., and T. O'Donoghue (2006), Response of sand ripples to change in oscillatory flow, *Sedimentology*, *53*, 581–596, doi:10.1111/j.1365-3091.2006.00774.x.
Gallagher, E. L., E. B. Thornton, and T. P. Stanton (2003), Sand bed roughness in the nearshore, *J. Geophys. Res.*, *108*(C2), 3039, doi:10.1029/2001JC001081.
Gallagher, E. L., S. Elgar, R. T. Guza, and E. B. Thornton (2005), Estimating nearshore bedform amplitudes with altimeters, *Mar. Geol.*, *216*, 51–57, doi:10.1016/j.margeo.2005.01.005.
Greenlaw, C. F., D. V. Holliday, and D. E. McGehee (2004), High-frequency scattering from saturated sand sediments, *J. Acoust. Soc. Am.*, *115*(6), 2818–2823, doi:10.1121/1.1707085.
Hanes, D. M., V. Alymov, Y. X. Chang, and C. Jette (2001), Wave-formed sand ripples at Duck, North Carolina, *J. Geophys. Res.*, *106*(C10), 22,575–22,592, doi:10.1029/2000JC000337.
Hay, A. E., and T. Mudge (2005), Primary bed states during SandyDuck97: Occurrence, spectral anisotropy, and the bed state storm cycle, *J. Geophys. Res.*, *110*, C03013, doi:10.1029/2004JC002451.
Hay, A. E., and D. L. Wilson (1994), Rotary sidescan images of nearshore bedform evolution during a storm, *Mar. Geol.*, *119*, 57–65, doi:10.1016/0025-3227(94)90140-6.
Henderson, S. M., and A. J. Bowen (2002), Observations of surf beat forcing and dissipation, *J. Geophys. Res.*, *107*(C11), 3193, doi:10.1029/2000JC000498.
Jenkins, G. M., and D. G. Watts (1968), *Spectral Analysis and Its Applications*, 525 pp., Holden-Day, San Francisco, Calif.
Madsen, O., P. Mathisen, and M. Rosengaus (1990), Movable bed friction factors for spectral waves, paper presented at 22nd Coastal Engineering Conference, Am. Soc. of Civ. Eng., Delft, Netherlands.
Maier, I., and A. E. Hay (2009), Occurrence and orientation of anorbital ripples in nearshore sands, *J. Geophys. Res.*, *114*, F04022, doi:10.1029/2008JF001126.
Meyer-Peter, E., and R. Müller (1948), Formulas for bed-load transport, in Report on the Second Meeting of the International Association for Hydaulic Structures Research, pp. 39–64, Int. Assoc. for Hydraul. Res., Stockholm.
Nielsen, P. (1981), Dynamics and geometry of wave–generated ripples, *J. Geophys. Res.*, *86*(C7), 6467–6472, doi:10.1029/JC086iC07p06467.
Nielsen, P. (1992), *Coastal Bottom Boundary Layers and Sediment Transport*, 324 pp., World Sci., River Edge, N. J.
Nolle, A. W., W. A. Hoyer, J. F. Mifsud, W. R. Runyan, and M. B. Ward (1963), Acoustic properties of water-filled sands, *J. Acoust. Soc. Am.*, *35*, 1394–1408, doi:10.1121/1.1918703.
Nuttall, A. H. (1971), Spectral estimation by means of overlapped fast Fourier transform processing of windowed data, *Tech. Rep. 4169*, Nav. Underwater Syst. Cent., Newport, R. I.
O'Donoghue, T., J. S. Doucette, J. J. van der Werf, and J. S. Ribberink (2006), The dimensions of sand ripples in full-scale oscillatory flows, *Coastal Eng.*, *53*, 997–1012, doi:10.1016/j.coastaleng.2006.06.008.
Pedocchi, F., and M. H. Garcia (2009), Ripple morphology under oscillatory flow: 1. Prediction, *J. Geophys. Res.*, *114*, C12014, doi:10.1029/2009JC005354.
Ribberink, J. (1998), Bed-load transport for steady flows and unsteady oscillatory flows, *Coastal Eng.*, *34*(1–2), 59–82, doi:10.1016/S0378-3839(98)00013-1.
Schlichting, H. (1979), *Boundary Layer Theory*, 7th ed., 817 pp., McGraw-Hill, New York.
Smith, D., and J. F. A. Sleath (2005), Transient ripples in oscillatory flows, *Cont. Shelf Res.*, *25*, 485–501, doi:10.1016/j.csr.2004.10.012.
Smyth, C., A. E. Hay, and L. Zedel (2002), Coherent Doppler Profiler measurements of near-bed suspended sediment fluxes and the influence of bed forms, *J. Geophys. Res.*, *107*(C8), 3105, doi:10.1029/2000JC000760.
Soulsby, R. L., and R. J. S. Whitehouse (1997), Threshold of sediment motion in coastal environments, in *Pacific Coasts and Ports '97: Proceedings of the 13th Australasian Coastal and Ocean Engineering Conference and the 6th Australasian Port and Harbour Conference*, vol. 1, Cent. for Adv. Eng., Univ. of Canterbury, Christchurch, New Zealand.
Soulsby, R. L., and R. J. S. Whitehouse (2005), Prediction of ripple properties in shelf seas: Mark 2 predictor for time evolution, *Tech. Rep. TR 154*, HR Wallingford, Wallingford, U. K.
Tang, D., K. R. Williams, and E. I. Thorsos (2009), Using high-frequency backscatter to estimate bottom sand ripple parameters, *IEEE J. Oceanic Eng.*, *34*(4), 431–443, doi:10.1109/JOE.2009.2015402.
Thornton, E. B., and R. T. Guza (1983), Transformation of wave height distribution, *J. Geophys. Res.*, *88*(C10), 5925–5938, doi:10.1029/JC088iC10p05925.
Traykovski, P. (2007), Observations of wave orbital scale ripples and a nonequilibrium time-dependent model, *J. Geophys. Res.*, *112*, C06026, doi:10.1029/2006JC003811.
Traykovski, P., A. E. Hay, J. D. Irish, and J. F. Lynch (1999), Geometry, migration, and evolution of wave orbital ripples at LEO-15, *J. Geophys. Res.*, *104*, 1505–1524, doi:10.1029/1998JC900026.
van der Veen, H. H., S. J. M. H. Hulscher, and M. A. F. Knaapen (2006), Grain size dependency in the occurrence of sand waves, *Ocean Dyn.*, *56*, 228–234, doi:10.1007/s10236-005-0049-7.
van Rijn, L. C. (1993), *Principles of Sediment Transport in Rivers, Estuaries and Coastal Seas*, Aqua, Amsterdam, Netherlands.
Voropayev, S. I., G. B. McEachern, D. L. Boyer, and H. J. S. Fernando (1999), Dynamics of sand ripples and burial/scouring of cobbles in oscillatory flow, *Appl. Ocean Res.*, *21*, 249–261, doi:10.1016/S0141-1187(99)00015-2.
Wiberg, P. L., and C. K. Harris (1994), Ripple geometry in wave-dominated environments, *J. Geophys. Res.*, *99*(C1), 775–789, doi:10.1029/93JC02726.

A. E. Hay, Department of Oceanography, Dalhousie University, 1355 Oxford St., Halifax, NS B3H 4JI, Canada. (alex.hay@dal.ca)